THE ASTROPHYSICAL JOURNAL, 516:349–365, 1999 May 1

PROSPECTS FOR MEASURING DIFFERENTIAL ROTATION IN WHITE DWARFS THROUGH ASTEROSEISMOLOGY

STEVEN D. KAWALER,[1,2] TAKASHI SEKII,[2] AND DOUGLAS GOUGH[2,3]
Received 1998 June 23; accepted 1998 December 8

ABSTRACT

We examine the potential of asteroseismology for exploring the internal rotation of white dwarf stars. Data from global observing campaigns have revealed a wealth of frequencies, some of which show the signature of rotational splitting. Tools developed for helioseismology to use many solar p-mode frequencies for inversion of the rotation rate with depth are adapted to the case of more limited numbers of modes of low degree. We find that the small number of available modes in white dwarfs, coupled with the similarity between the rotational-splitting kernels of the modes, renders direct inversion unstable. Accordingly, we adopt what we consider to be plausible functional forms for the differential rotation profile; this is sufficiently restrictive to enable us to carry out a useful calibration. We show examples of this technique for PG 1159 stars and pulsating DB white dwarfs. Published frequency splittings for white dwarfs are currently not accurate enough for meaningful inversions; reanalysis of existing data can provide splittings of sufficient accuracy when the frequencies of individual peaks are extracted via least-squares fitting or multipeak decompositions. We find that, when mode trapping is evident in the period spacing of g modes, the measured splittings can constrain $d\Omega/dr$.

Subject headings: stars: individual (PG 1159−035, GD 358) — stars: oscillations — stars: rotation — white dwarfs

1. INTRODUCTION

In recent years, the study of the late evolutionary stages of low- and intermediate-mass stars has benefited significantly from the investigation of pulsating white dwarfs. There are three classes of pulsating white dwarf stars: the pulsating DA white dwarfs (ZZ Ceti stars), the pulsating DB white dwarfs (i.e., GD 358), and the hot, C/O rich GW Vir (or pulsating PG 1159) stars. Through asteroseismological analysis of their pulsations, we have learned about their global properties (mass, luminosity, effective temperature, distance, rotation periods, etc.) and their internal properties (compositional stratification, cooling rates, magnetic field strength, etc.). Examples of the best-studied pulsating white dwarfs include PG 1159−035 (Winget et al. 1991, hereafter WWETPG; Kawaler & Bradley 1994), the pulsating DB white dwarf GD 358 (Winget et al. 1994; Bradley & Winget 1994), and the ZZ Ceti star G29-38 (Kleinman et al. 1998); see also the reviews contained in proceedings of the Whole Earth Telescope Workshops (Meistas & Solheim 1996; Meistas & Moskalik 1998). As the observational situation has improved, most notably with the continuing work of the Whole Earth Telescope (WET; Nather et al. 1990), there now exists the possibility for even more detailed probing of these stars. For example, Winget et al. (1994, hereafter WWETDB) report that the power spectrum of GD 358 shows evidence for a variation of rotation with depth and of a modest magnetic field. In this paper, we explore the possibilities of using the measured pulsation frequencies to constrain internal rotation profiles.

Traditional determination of rotation rates in stars involve measuring rotational broadening of spectral lines. In white dwarfs, the natural broadening mechanisms render such rotational broadening measurements insensitive to rotation periods longer than a few hours. In some cases, narrow Balmer-line cores can be produced by non-LTE (NLTE) effects (see § 1.2 below), but ambiguity between NLTE subtleties and rotational broadening complicates their interpretation (i.e., Koester et al. 1998). Fortunately, one of the properties that can be provided by pulsation observations is the rotation of the star. A frequently used relation between the observed frequency splitting and the angular velocity Ω of the star, valid when Ω is constant (and small compared with $2\pi\nu_{nl}$), is

$$m\,\delta\nu_{nl} \equiv \nu_{nlm} - \nu_{nl0} = \frac{m}{P_{\rm rot}}\,\beta_{nl}\,, \tag{1}$$

where ν_{nl0} is the cyclic frequency of oscillation of a mode of order n and degree l in the absence of rotation, ν_{nlm} is the observed frequency for a given multiplet component with azimuthal quantum number m, and $P_{\rm rot}$ is the rotation period of the star. The quantity β_{nl} is a function of the oscillation eigenfunction of the corresponding nonrotating stars and is independent of m; for g modes of white dwarf stars, a useful approximation, good to about 10% and frequently much better, is

$$\beta_{nl} \approx 1 - \frac{1}{l(l+1)} \tag{2}$$

(Brickhill 1975). Another form for the rotation splitting constant is C_{nl}, where $C_{nl} = 1 - \beta_{nl}$.

Equation (1) assumes that the angular velocity $\boldsymbol{\Omega}$ is constant throughout the star. However, there is no reason a priori to believe that white dwarfs rotate uniformly. If the putative variation of the angular velocity with depth is taken into account, the resulting rotational splitting is

$$\delta\nu_{nl} = 2\pi I^{-1}\int_0^R \Omega(r)\left\{\xi^2 + 2\xi\eta + \left[1 - \frac{1}{l(l+1)}\right]\eta^2\right\}\rho r^2\,dr\,, \tag{3}$$

[1] Department of Physics and Astronomy, Iowa State University, Ames, IA 50011; sdk@iastate.edu.
[2] Institute of Astronomy, University of Cambridge, Madingley Road, Cambridge CB3 0HA, England.
[3] Department of Applied Mathematics and Theoretical Physics, University of Cambridge, Silver Street, Cambridge CB3 9EW, England.

where ξ and η represent the amplitudes of the vertical and horizontal displacement eigenfunctions, ignoring the perturbation due to rotation. The normalization factor I is the inertia of the mode. It is given by

$$I = \int_0^R [\xi^2 + \eta^2]\rho r^2 \, dr \, . \tag{4}$$

For typical observable g modes in white dwarf stars, $n \gg l$, and therefore $\eta \gg \xi$; it is in the limit $l/n \to 0$ that the rotational coefficient β_{nl} for uniform rotation reaches the asymptotic value given by equation (2). As in equation (1), equation (3) for the mean splitting $\delta\nu_{nl}$ is also independent of m.

The rotational splitting formula (eq. [3]) represents a weighted average of the rotation rate with depth. A single splitting therefore provides us with only some average rotation rate, weighted by the displacement eigenfunction of the mode in question. It is convenient to rewrite equation (3) as follows:

$$\delta\nu_{nl} = 2\pi \int_0^R K_{nl}(r)\Omega(r) \, dr \, , \tag{5}$$

where the data kernel (weighting function) $K_{nl}(r)$ depends on the rotationally unperturbed eigenfunction for the mode specified by n and l and is a function of r alone. Note that the normalization of K_{nl} is such that the integral of K_{nl} is β_{nl}, which for most of the modes considered in this paper is approximately 0.5. The rotation kernels are available from the pulsation analysis of a representative equilibrium stellar model. Constraints on possible stellar models can be applied from the observed frequencies of oscillation and, in principle, can limit the possibilities adequately, allowing us then to interpret the observed splitting in somewhat more detail than identifying some "average rotation rate of the star."

1.1. *Toward Determining Differential Rotation*

When several rotational splittings have been measured in a star, the appropriate kernels for the modes observed can be used to constrain the depth dependence of the rotation rate. Such constraints can be obtained by two procedures: forward calculation and inversion. In the forward procedure, the observed splittings are reproduced using the best available stellar model by adjusting the model internal rotation rate (somehow) to match the observed frequency splittings. However, if a function $\Omega(r)$ can be found to produce a good match, then there are many—formally infinitely many—other functions $\Omega(r)$ that can do so too. Moreover, it does not guarantee a straightforward analysis of the effects of observational errors, although Monte Carlo methods can easily be used. The forward calculation is a useful elementary way to explore the property of classes of "solutions" (such as power laws, flat rotation curves, etc.) and is relatively fast to compute. In most analyses that have been carried out to date, rotational splittings are converted into rotation rates by assuming a flat rotation curve and using equation (1) or its equivalent.

The object of inversion is to "solve" equations (5), using all the observed rotational splittings and kernels from an appropriate stellar model, to obtain values of Ω in different regions of the stellar interior. Evidently, with only a finite number of data, no unique function $\Omega(r)$ can be determined. Consequently additional constraints must be applied to render the solution unique. A natural constraint imposes smoothness, since by their nature typical kernel sets cannot isolate small-scale structure.

Rotational inversion procedures have been explored extensively in the context of helioseismology and have yielded quite detailed mapping of the sun's angular velocity as a function of depth and latitude. We refer the reader to review by Gough & Thompson (1991), and references therein, for the details. Here we point out simply that the procedures fall basically into two categories. In the first, a class of acceptable (typically smooth) functions $\Omega(r)$ satisfying equation (5) (within the observational uncertainty) is sought. One that is considered to be best is chosen, based on a criterion that balances satisfying the data and satisfying the externally imposed acceptability criterion (such as smoothness). This method emphasizes reproducing the data and is logically just a formalization of the search in the forward method mentioned above. The other method is directed toward addressing actual properties of the rotation, rather than satisfying the data. It seeks linear combinations of data that yield equations of the type of equation (5) but with more easily interpretable kernels (such as kernels that are highly localized in space and are nowhere [large and] negative). The outcome of this method is simpler to interpret, since the results are local averages over known regions. However, it is not always possible to construct an averaging kernel with the desired properties unless the data kernels associated with the data are sufficiently diverse that localized information is unambiguously contained in the data. That is not the case of the data we discuss in this paper. It is therefore prudent to adopt a method from the first category. Helioseismic data contain the signals of millions of frequencies, over a range of degree up to and above $l = 1000$. For white dwarfs, however, l is typically 1, and occasionally 2. Stars considered to be "rich" pulsators show 20 separate multiplets. Thus the prospect for detailed rotational inversion for white dwarfs is limited. We note that Goupil et al. (1996) explored some inversion techniques for δ Scuti stars, which pose similar observational problems.

1.2. *Rotation in White Dwarf Stars*

We have much to learn about the global properties, let alone the detailed interior properties, of white dwarfs. Surface rotation rates are known for a very small number of white dwarfs. Rotational broadening in even rapidly rotating white dwarfs is difficult to measure; only in a few cases is there a sharp NLTE core in the hydrogen lines in which the effects of rotation may be detected (Pilachowski & Milkey 1984; Koester et al. 1998). Magnetic white dwarfs occasionally show rotational modulation (Schmidt 1995). Fortunately, rotation is relatively easy to measure in the pulsating white dwarfs; indeed, the most accurate measures of white dwarf rotation have come from pulsation. Furthermore, a simple demonstration that pulsating white dwarfs do not rotate as solid bodies in their interiors would be the first such direct demonstration for stars other than the Sun. Even a coarse measure of differential rotation can provide important constraints on the prior evolution of a white dwarf and on conditions in the interior of its progenitor.

In this paper, we examine the prospects of measuring differential rotation in white dwarf stars using asteroseismic

data. We find that we can indeed place important constraints on the internal rotation of stars such as PG 1159, PG 2131, and GD 358. With anticipated improved accuracy in the measured rotational splitting of g-mode frequencies, we may indeed see the clear signature of differential rotation. In the next section, we explore the expected splittings for a variety of rotation laws through forward calculations. It is important to illustrate a variety of examples in order to provide some sense of the sensitivity of the frequency splitting to Ω and, hence, of the diagnostic power of the splitting data. The subsequent section reviews the methods for rotational inversion that have been used with some success in helioseismology, and which can be adapted to the study of white dwarf stars. Section 4 shows examples of how these methods work for models of PG 1159 stars and DBV stars with the synthetic rotational splittings from § 2. In § 5 we apply these methods to the published splittings for PG 1159 and GD 358 stars. We illustrate the difficulties that are encountered in using the splittings to constrain the actual rotation rates, and we suggest a model-independent technique for estimating $d\Omega/dr$. We conclude in § 6 with prospects for the future progress.

2. ROTATIONAL SPLITTINGS OF OSCILLATION FREQUENCIES FOR VARIOUS ROTATION PROFILES: THE FORWARD PROBLEM

In the forward problem, equation (5) is used to compute the expected splittings for a given value of $\Omega(r)$. In practice, the integral is replaced by an appropriate finite-difference representation, and the kernels and the angular velocity are evaluated over a grid in r. In pre–white dwarfs, as in the Sun, radius provides a good independent variable, as the rotation kernels are evenly sampled throughout the star for modes of interest. In the pulsating DB models, radius evenly samples the kernels in the outer layers, where their amplitudes are largest (see Figures 1 and 2).

If there are M independent splittings measured, then equation (5) becomes

$$\delta\nu_i = \sum_{j=1}^{N} w_j K_{ij} \Omega_j \quad i = 1 \ldots M \,, \tag{6}$$

where the index j corresponds to the radial mesh point in the model, w_j is a weight that depends on the difference scheme adopted, and the index i labels the specific splitting.

In this section, we use equation (6) to explore how $\delta\nu_i$ depends on various rotation laws, using kernels computed from models of PG 1159 and GD 358. This provides some insight into the sort of signal that is to be expected from white dwarf stars. We shall then use these synthetic splittings in the subsequent sections to test various inversion procedures.

Figure 1 shows representative rotation kernels computed from a model by Kawaler & Bradley (1994) of the hot white dwarf PG 1159. The selection of overtones spans the pulsation modes observed in this star by WET. Note that the rotation kernels are remarkably similar and that they have

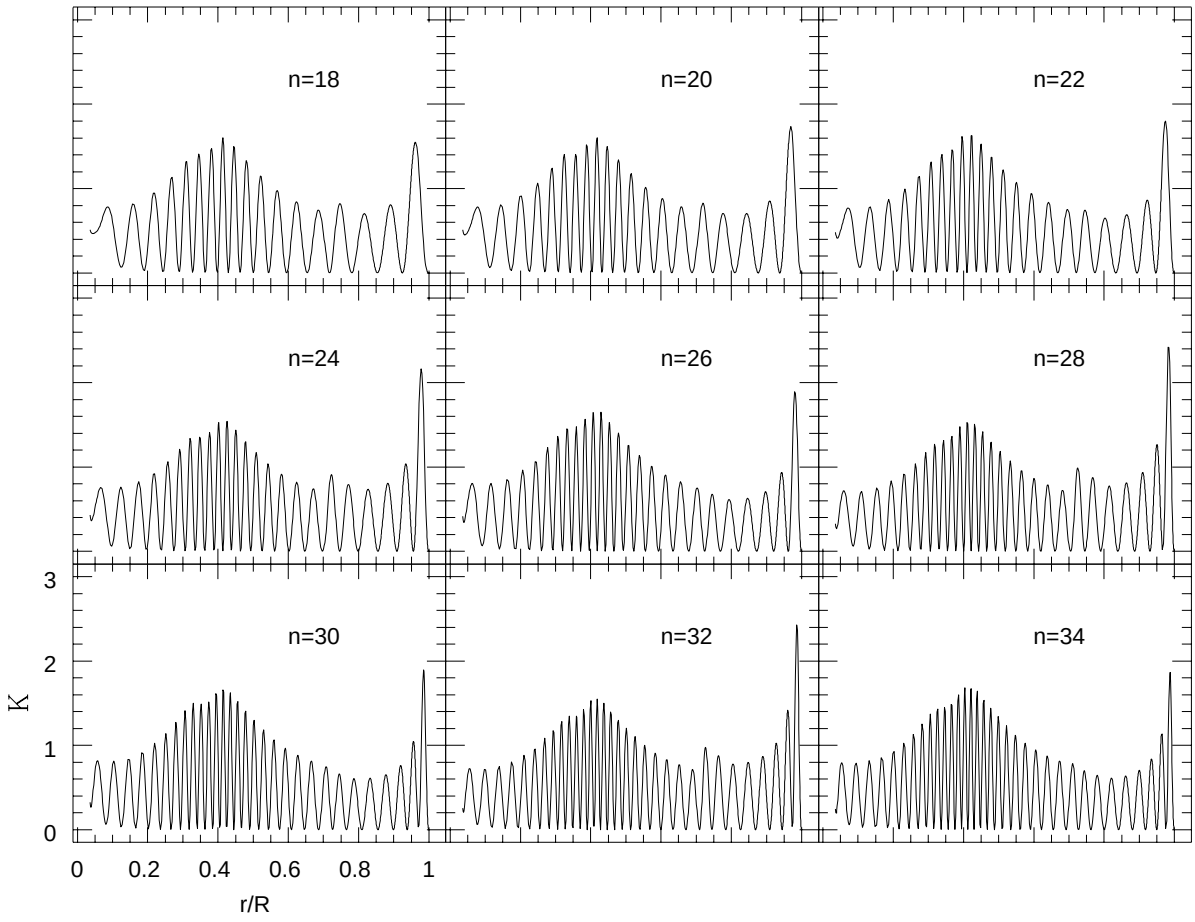

FIG. 1.—Sample rotation kernels $K_n(r)$ of $l = 1$ g-modes in a model of PG 1159. As described in the text, the kernels are normalized by the kinetic energy of the mode.

significant amplitude over the entire stellar interior. As discussed in Kawaler et al. (1985), stars like PG 1159 are indeed pre–white-dwarf stars; while their interiors are degenerate, the Brunt-Väisälä frequency is not insubstantial, and the pulsation amplitude in the interior, while smaller than that at the surface, is much larger than it is in cool white dwarf stars. The similarity amongst these kernels renders localization extremely difficult, if not impossible, and severely limits the power of inversion techniques to resolve the rotation profile.

Figure 2 shows rotation kernels for a model of the pulsating DB white dwarf star GD 358, plotted in just the outer 20% by radius of the star. In this model, the eigenfunctions are relatively much smaller in the stellar interior: the modes corresponding to the observed frequencies sense the rotation mainly in the outer layers of the star. Note that the kernel amplitude changes dramatically from mode to mode; this is a manifestation of mode trapping. The composition transition between pure helium near the surface and the C- and O-rich core (which extends to a fractional radius of 0.98) is sufficient to pinch those eigenfunctions that have small vertical displacements at the transition. These modes have substantially smaller amplitudes below the transition, and their kernels therefore have much larger surface values. From inspection of Figure 2, it is apparent that the trapped modes have $n = 9$,10, and $n = 15$,16.

Mode trapping is also present in the PG 1159 model, caused by a composition transition at $r/R = 0.72$. In the kernels shown in Figure 1, this results in a small bump in the kernels for $n = 20$, 24, 28, and 32 at that radial position—these are the trapped modes. For PG 1159 stars, the influence of mode trapping on the pulsation spectrum and, in particular, on the spacing in period of g-modes, is discussed by Kawaler & Bradley (1994, and see below).

As long as Ω changes smoothly, the rotational splittings that result depend principally on the envelopes of the kernels. Since these are quite similar for all modes in Figure 1, and all modes in Figure 2, save for the relatively minor evidence for trapping, detailed inversion is bound to be difficult.

2.1. *PG 1159 Stars*

As a first example, we consider the uniform rotation profile with $\Omega/2\pi = 10$ μHz. The spacing of the triplet dipole components are shown in the top panel of Figure 3. Note that the splittings are not constant; this is a measure of the departure of the splittings from the approximation given by equation (2) and results from the influence of the vertical displacement on the phase retardation produced by the Coriolis force in the rotating frame. The values do indeed approach the asymptotic limit (eq. [2]) as n increases.

The middle panel in Figure 3 shows the splittings (joined by continuous lines) that result from a rotation rate that decreases linearly with radius from 20 μHz at the center to 0 μHz at the surface; note that although this curve has a

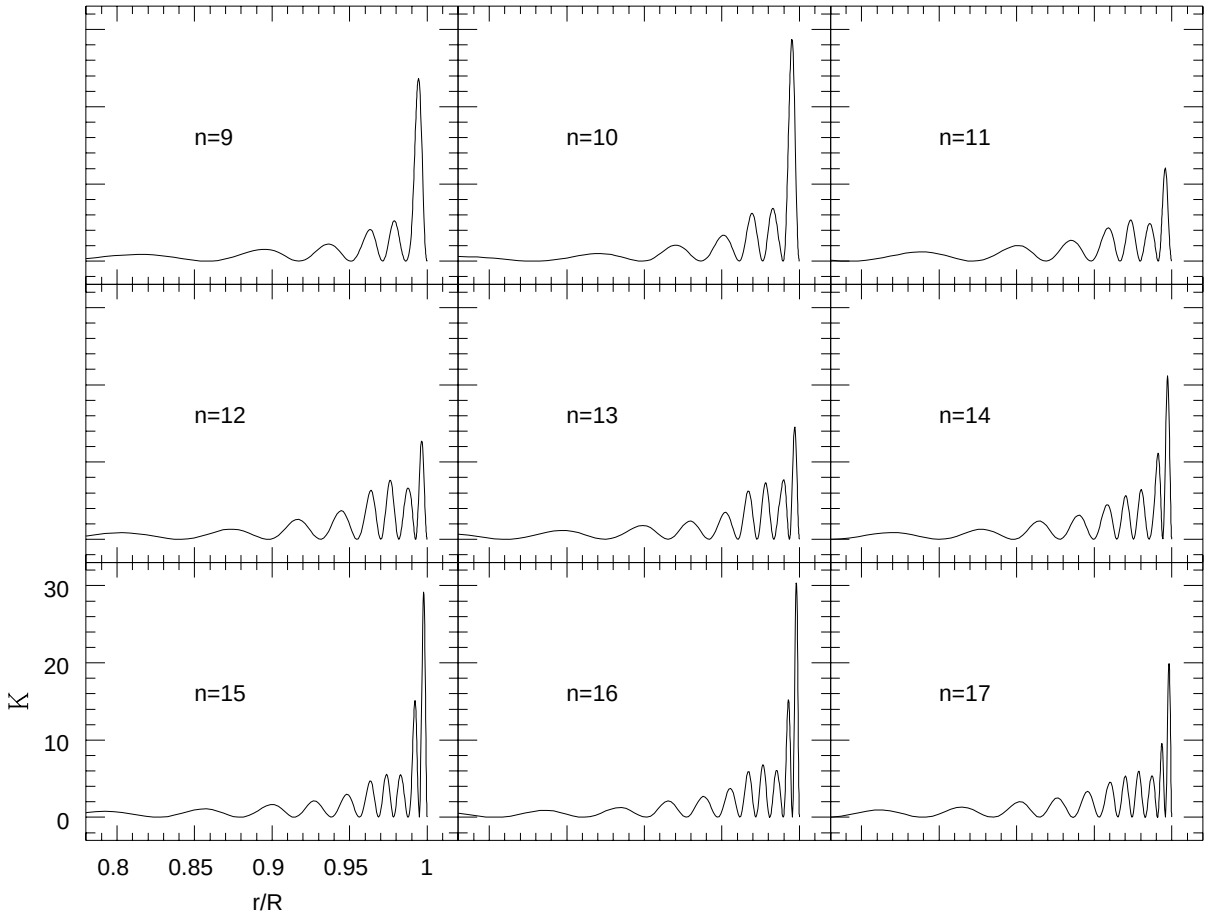

FIG. 2.—Sample rotation kernels $K_n(r)$ of $l = 1$ g-modes in a model of GD 358. Only the outer 20% of the radius is shown; the amplitude of the kernel is very small in the interior. Note that the amplitude of the kernel in the outer layers is a strong function of n; this is the consequence of mode trapping.

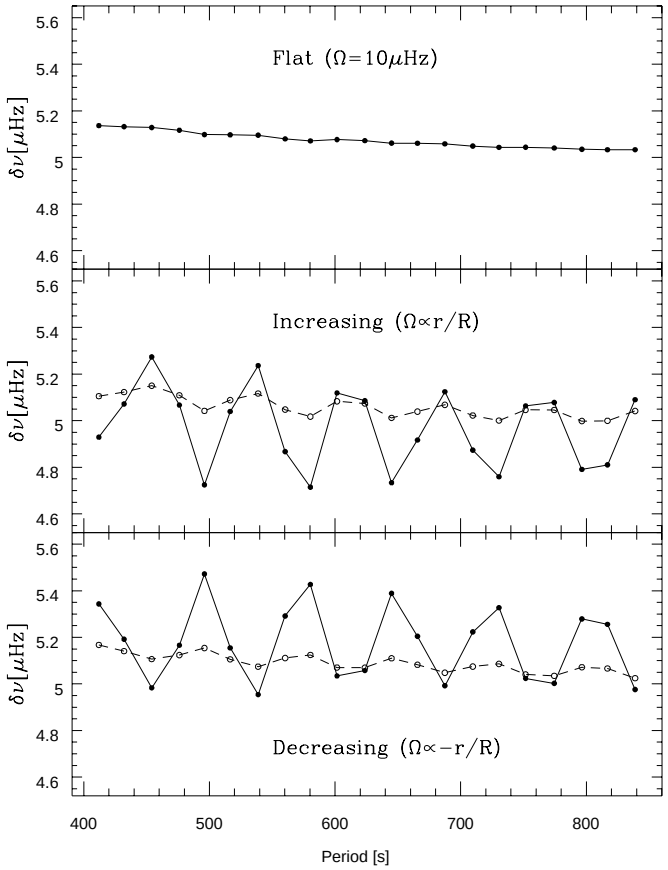

FIG. 3.—Rotational splitting (in μHz) for the PG 1159 model with various forms for $\Omega(r)$. *Top panel*: Flat rotation curve, with $\Omega = 10$ μHz. *Middle panel*: Linearly decreasing rotation curve with a small slope in $\Omega(r)$ (*dashed line*) and a steep slope in $\Omega(r)$ (*solid line*). *Bottom panel*: Linearly increasing rotation rate with a small slope (*dashed line*) and a steep slope (*solid line*).

mean value of a little more than 5 μHz, as does the uppermost panel, the splittings vary substantially about that mean. The dashed lines in this panel join splittings for another rotation profile that decreases linearly with radius, but with a shallower slope (from 11.5 μHz at the center to 8.5 μHz at the surface). In this case, the variations have much smaller amplitude, but they have exactly the same phase as those produced by the steeper profile. The bottom panel is similar to the middle panel but shows the splittings for two cases in which the rotation rate increases linearly with radius. Notice that the sign of the oscillations about the smoother dashed curve is reversed.

The periodic variations of the rotational splitting are the consequence of mode trapping. Subsurface composition transitions can trap some nonradial modes between the transition zone and the surface. The composition gradient leads to a density gradient, which acts as a reflecting boundary. Modes with radial displacement eigenfunctions that are close to zero near the transition are pinched at that point and have nearly zero amplitude below. Because such trapped modes are confined in the outer nondegenerate layers, they have substantially smaller kinetic energies at given surface amplitude than do similar nontrapped modes. Mode trapping manifests itself in reduced period spacings; in general, the trapping pushes trapped modes to longer periods (Kawaler & Bradley 1994). The observational diagnostic of trapped modes is the occurrence of local minima in the period spacing considered as a function of period. Figure 4 shows that spacing as a dashed line; the rotational splittings for the case of a linear decreasing rotation rate are shown by filled circles connected by continuous lines. Clearly, the rotational splittings show the signature of mode trapping. Since trapped modes are more confined to the surface, they are more sensitive to rotation in the outer layers. For a radially decreasing rotation profile, the trapped modes exhibit minima in the rotational splitting.

Another forward calculation of rotational splitting for the PG 1159 model is shown in Figure 5. In this calculation, we computed the rotational splitting for two different forms of a decreasing rotation law: one that decreases linearly with radius and another that decreases as a power law in r/R. The splittings exhibit the characteristic structure of a rotation rate that decreases outward. Despite the rather different rotation laws, the general forms of $\delta\nu$ as a function of period for both rotation law are strikingly similar. The values of the parameters of these rotation curves were chosen to match the mean value of the rotational splittings of the two cases. The maximum difference in splitting is only about 0.03 μHz. The reason for their similarity is simply that the oscillatory behavior of the splittings is a product principally of the rotationally unperturbed eigenfunctions and not of the detailed form of $\mathbf{\Omega}$. This illustrates that the influence of mode trapping is similar for these two rotation curves, both of which decrease with radius. Thus the observed phase between the rotational splitting and the period spacings provides an observational determination of the sign of the slope of the rotation curve. While the splittings can indicate that the rotation rate decreases outward, we expect that the observed values will, for PG 1159 stars, be inadequate for detailed constraints on the form of the rotation law.

2.2. *Pulsating DB White Dwarfs*

We used the same rotation laws in the models of GD 358 to see the response of the rotational splittings. In this case the response to a flat rotation curve is very similar to the case for PG 1159 models above; the splittings are shown as the middle (*solid*) line in Figure 6 for a flat rotation curve

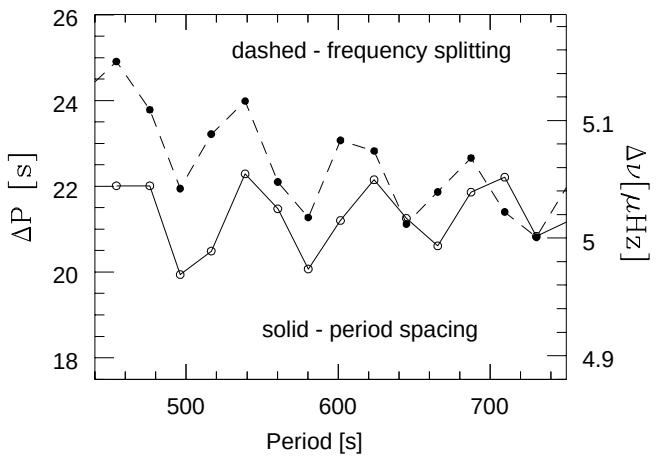

FIG. 4.—Period spacing as a function of period in the representative PG 1159 model (*solid line*), with values indicated on the left axis. The dotted line shows the rotational splitting computed with a linearly decreasing rotation curve (see Fig. 3), with values indicated on the right axis.

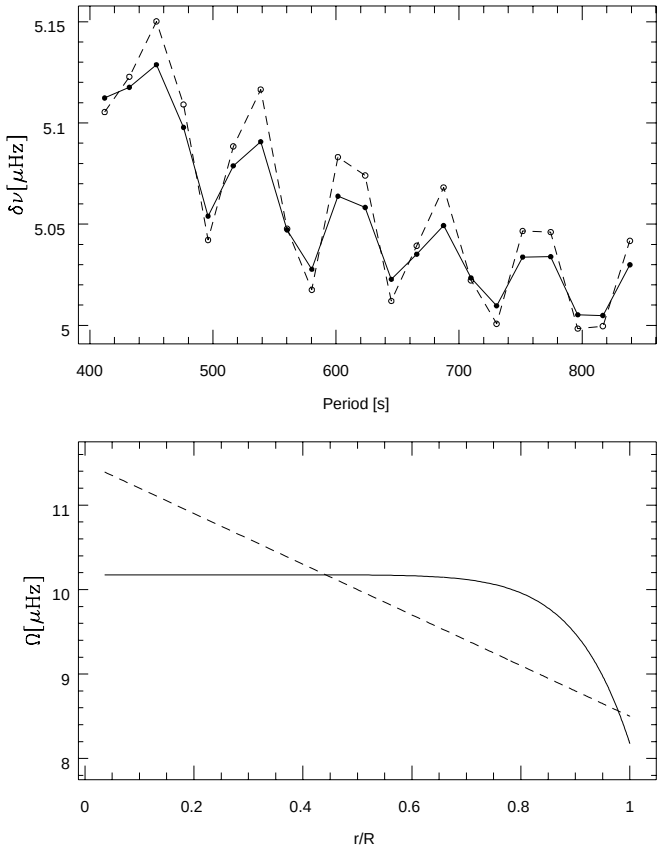

FIG. 5.—*Upper panel*: Rotational splittings computed for a PG 1159 model with a rotation curve that decreases linearly with radius (*dashed line*; see middle panel of Fig. 3) compared with the splittings for a rotation curve that follows a power law (*solid line*). *Lower panel*: Rotation rates for the two models.

with $\mathbf{\Omega}$ of 10 μHz. The splittings for $\mathbf{\Omega}$ decreasing linearly from 11.5 μHz at the center to 8.5 μHz at the surface are shown in Figure 6 by the bottom (*solid*) line; the top (*dashed*) line shows splittings for a rotation rate that increases linearly from 8.5 μHz at the center to 11.5 μHz at the surface.

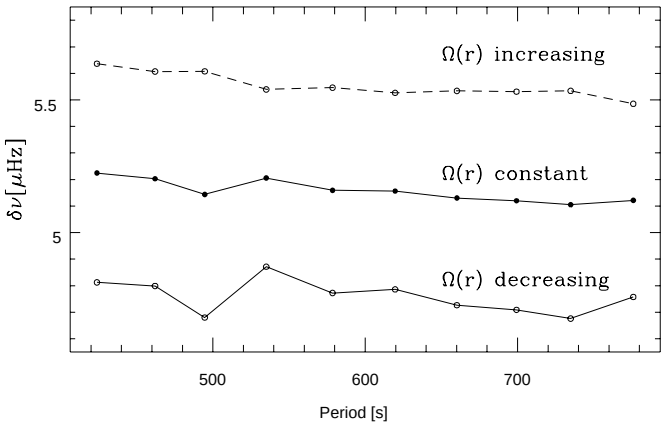

FIG. 6.—Rotational splittings for modes in the model of GD 358. The solid lines show the splittings for a flat rotation curve with a rotation rate of 10 μHz. The top dashed line shows splittings for a rotation curve that increases linearly with radius, while the bottom line shows that for a rotation rate that decreases linearly. All three rotation curves have the same mean values (mean with radius).

A glance at Figure 2 shows that the kernels in the GD 358 models sample the outer layers much more strongly than the core, unlike the PG 1159 kernels, which sample the whole star. Thus a linear decrease in $\Omega(r)$ results in an overall shift downward for the splittings, as the surface layers in this case are all at a lower value of $\mathbf{\Omega}$ when the mean value of $\mathbf{\Omega}$ remains unchanged. Similarly, splittings computed for a rotation law that increases with increasing r are displaced upward. Beyond this overall displacement, however, this simple form for the rotation law results in only subtle changes in the value of $\delta\nu$ as a function of period. Linear rotation laws change by only a few percent across the region where the kernels are large. Nevertheless, the slight differences between the splittings of the varying and constant rotation profiles reverse as the gradient of Ω is reversed, as for the PG 1159 stars.

Figure 7 shows the rotational splittings for a rotation rate that is the same as shown in Figure 5 for the PG 1159 model; that is; flat near the center and then decreasing as r/R to the tenth power to reach a surface value 2 μHz smaller. The central rate was adjusted again to give splittings nearly the same as for the case of a linearly decreasing rotation curve. As in the case for the PG 1159 model, the rotational splittings are very similar; they show the same pattern for decreasing rotation curves and differ by small amounts only. Thus for GD 358 stars too, it may also be difficult to attain the necessary accuracy for detailed study of the rotation rate with depth unless very high accuracy frequencies are available. As we see below, the results of

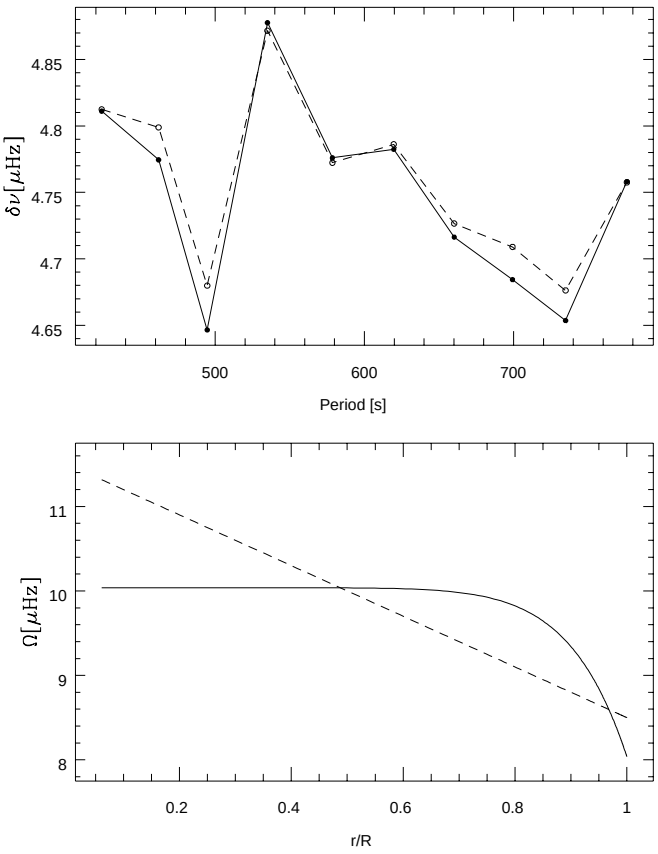

FIG. 7.—*Upper panel*: Rotational splittings computed for a GD 358 model with a rotation curve that decreases linearly with radius (*dashed line*) compared with the splittings for a rotation curve that follows a power law (*solid line*). *Lower panel*: Rotation rates for the two models.

inversions are very sensitive to errors in the measured splittings, as is clear from the results of these forward calculations.

3. ROTATIONAL INVERSION TECHNIQUES

In exploring inversion procedures, we borrow heavily from the field of helioseismology. An extensive literature on the inverse problem for solar rotation exists; as an example, see Gough (1985) and Christensen-Dalsgaard, Schou, & Thompson (1990). In this section we assess several procedures, in use in studies of the solar internal rotation, for possible adaptation to leuconanoseismology. In the process, we illustrate how the restrictions imposed by the observational limitations make very different demands on the numerical procedures from those in the solar case. We conclude this section by suggesting a technique for using inversion theory to best advantage for white dwarfs.

3.1. *Direct Inversion*

Direct solution of the integral equation (5) or its discrete analog equation (6) (one knows the splittings from observation and the kernels from theory) can in principle yield $\Omega(r)$. The system of M equations contains N unknowns (the values of $\boldsymbol{\Omega}_j$). Hence, unless the number of measured splittings is greater than the number of resolution points of $\Omega(r)$, the system of equation is (formally) underdetermined.

In such situations (particularly where $M \ll N$), $\Omega(r)$ need further constraint. As described earlier, additional information must be provided. Alternatively the function space may be restricted by imposing, for example, a degree of smoothness (see the discussion of regularization below). In the opposite case, $M > N$ (such as is frequently the case for the Sun), we cannot guarantee to satisfy all the splitting constraints. Under this circumstance we appeal to the χ^2 statistic, and the function $\Omega(r)$ that minimizes χ^2 for the inverted splittings is sought (this is what is usually called least-squares fitting). Forming χ^2 as the sum of squares of the differences between the measured splittings and those computed with the putative solution $\Omega(r)$, weighted with the inverse square of the standard errors σ_i (we presume here that the errors in the measurement are independent), the minimum in χ^2 is attained when

$$\sum_i \frac{1}{\sigma_i^2}\,\delta v_i\, w_j\, K_{ij} = \sum_i \frac{1}{\sigma_i^2}\, w_j\, K_{ij} \sum_k w_k\, K_{ik}\, \Omega_k \qquad j = 1 \ldots N\ . \tag{7}$$

In matrix form, this equation is

$$\boldsymbol{K}^T \frac{\delta v}{\sigma} = \boldsymbol{K}^T \boldsymbol{K} \boldsymbol{\Omega}\ , \tag{8}$$

where $(\boldsymbol{K})_{ij} = w_j K_{ij}/\sigma_i$. This is an $N \times N$ system, the solution of which provides the values of $\boldsymbol{\Omega}_i$ that minimize the error-weighted residuals between the observed splittings and those obtained using $\Omega(r)$ in the forward problem.

As it stands, the equation above is difficult to solve. If $M < N$, the matrix $\boldsymbol{K}^T\boldsymbol{K}$ is singular. And even if $M > N$, the matrix is very nearly singular because the envelopes of the kernels are similar. This singular nature is not particular to white dwarfs but is inherent in most inversions in general.

3.2. *Direct Inversion with Regularization*

To stabilize the solution obtained by least-squares fitting, we must impose additional conditions on the solution. If this could be accomplished in a physically sensible way, the outcome could be a rotation curve that is realistic. However, without a reliable dynamical theory, such imposition is out of reach.

Instead we resort to regularization, which involves adding extra terms to the right-hand side of equation (8) to penalize wild behavior of $\Omega(r)$:

$$\boldsymbol{K}^T \frac{\delta v}{\sigma} = (\boldsymbol{K}^T \boldsymbol{K} + \lambda \boldsymbol{H}) \boldsymbol{\Omega}\ . \tag{9}$$

The form of the $N \times N$ regularization matrix $\boldsymbol{H}$ determines what is penalized. For example, to penalize a steep gradient in $\Omega(r)$, $\boldsymbol{H}$ is chosen in such a way that $\boldsymbol{\Omega}^T \boldsymbol{H} \boldsymbol{\Omega}$ represents, e.g., the squared integral of $d\Omega/dr$ in a finite difference scheme (first-derivative smoothing). In this case it is found that $\boldsymbol{H} = \boldsymbol{D}^T \boldsymbol{D}$, where the matrix $\boldsymbol{D}$ is a discretized differential operator (Hansen, Sekii, & Shibahashi 1992). In other words, the regularization matrix $\boldsymbol{H}$ contains terms along (and parallel to) the diagonal. (To obtain approximate first-derivative smoothing, for example, the matrix $\boldsymbol{D}$ is everywhere zero except for a line of elements of value h_j immediately above the principal diagonal and another line of value $-h_j$ immediately below the principal diagonal, where $h_j = 1/[2(r_{j+1} - r_j)]^{1/2}$.) The regularization parameter λ is tunable; setting it to zero recovers the unstable least-squares formulation. In practice, numerical experimentation with different values of λ provides the inverter with the information to choose an optimal value, which provides a compromise between undue susceptibility to data errors and excessive smoothness.

The regularized least-squares fitting technique can be valuable, provided that it is appreciated how the regularization artificially constrains the solution. However, the results can be dreadfully unphysical, especially in the presence of noise—in the raw form of the procedure, no a priori limitations on the value of $\Omega(r)$ are made outside of the regularization, and with inadequate data it may provide the dominant influence on the form of the solution.

3.3. *Inversion onto a Fixed Functional Basis: "Function Fitting"*

The limited information currently available from oscillation of white dwarf stars is adequate to determine only a very few properties of $\Omega(r)$. As we show in § 4, attempts at regularized least-squares inversions with realistic simulations can yield markedly unrealistic results if the actual rotation rate does not conform to the regularization. Making explicit assumptions about the form of the rotation law (e.g., that it be positive definite, and that it either increases or decreases monotonically), we can at least restrict the class of acceptable functions in an easily comprehensible way. We term this "function fitting."

One way in which this can be accomplished is to consider projections of $\Omega(r)$ onto a fixed set of basis functions. Assume that the angular velocity in a white dwarf follows the general functional form

$$\Omega(r_j) = \sum_{k=1}^{K} a_k\, F_k(r_j)\ , \tag{10}$$

where the F_k are a set of K functions, evaluated of the N radii r_j, and a_k are coefficients to be evaluated. For example, if the $\Omega(r)$ were assumed to be a simple polynomial in r, the

functions F_k would be r^{k-1}. The splitting for multiplet i is then

$$\delta\nu_i = \sum_{j,k} K_{ij} w_j F_{jk} a_k \,, \tag{11}$$

where $F_{jk} = F_k(r_j)$, from which we form a new matrix $\boldsymbol{A}_{ik} = \Sigma_j \sigma_i^{-1} K_{ij} w_j F_{jk}$, which operates directly on the coefficients a_k. Then the system becomes, in matrix notation,

$$\boldsymbol{A}^T \frac{\delta\nu}{\sigma} = (\boldsymbol{A}^T\boldsymbol{A})\boldsymbol{a} \,, \tag{12}$$

which is solved for the k elements of $\boldsymbol{a}$ in terms of the observed splittings. The coefficients $\boldsymbol{a}$ then provide that rotation curve, of the form specified by the equation (10), which fits the data best (in the least-squares sense).

Of course the inversion discussed in § 3.1 falls into this category, with F_k being piecewise constant functions, but since we have in mind using only a very few such functions we prefer to add the flexibility of having a more general basis. We have explored only the very few bases enumerated below.

1. Simple polynomials of degree $K-1$:

$$\Omega(r) = \sum_{k=1}^{K} a_k (r/R)^{k-1} \,; \tag{13}$$

2. two linear segments, one with zero slope, joined at $r = r_b$:

$$\Omega(r) = \begin{cases} \boldsymbol{\Omega}_0 + \alpha(r_b - r)/R \,, & r < r_b \\ \boldsymbol{\Omega}_0 + \beta(r - r_b)/R \,, & r \geq r_b \end{cases}, \tag{14}$$

with either $\alpha = 0$ or $\beta = 0$;

3. a constant plus power of radius:

$$\Omega(r) = \boldsymbol{\Omega}_0 + \alpha(r/R)^q \tag{15}$$

or

$$\Omega(r) = \boldsymbol{\Omega}_0 + \alpha(1 - r/R)^{-q} \,, \tag{16}$$

where q is positive;

4. piecewise constant functions with a single break:

$$\Omega(r) = \begin{cases} \boldsymbol{\Omega}_1 \,, & r < r_b \\ \boldsymbol{\Omega}_2 \,, & r \geq r_b \end{cases}, \tag{17}$$

Inversions onto these bases are not linear, for all the bases are specified by a parameter that cannot be incorporated into the vector $\boldsymbol{q}$. In the polynomial and power-law cases, this parameter is the degree $K-1$ of the polynomial or the power q. In the forms with breaks, the parameter is r_b. To find the best values for these parameters, we minimize χ^2 over a range of the nonlinear parameter and select the solution with the smallest minimum χ^2 (see the next section).

4. ROTATIONAL INVERSIONS OF MODEL SPLITTINGS

The results from the forward calculations in § 2 hinted that inversion procedures will be sensitive to the modes measured and the accuracy with which the splittings are measured. In addition, the results must depend on the accuracy of the initial equilibrium model in comparison with the star itself. To explore these issues, we now calculate inversions using the various inversion procedures described above. We examine how they perform with the synthetic splittings computed in § 2. We shall discuss inversions of both error-free simulated data and simulations that include errors in splittings.

4.1. *Inversion of Splittings with No Errors*

As discussed in § 3, direct inversion is an inherently unstable calculation; some additional constraints are needed. To illustrate this point, consider the flat rotation curve for the PG 1159 model. Using all of the rotational splittings, a very small value for the regularization parameter λ of 10^{-4}, and a regularization matrix corresponding to smoothing of the first and second derivatives, the inverted rotation profile is shown as a solid line in Figure 8. The oscillatory behavior of $\Omega(r)$ with r is a sign that the numerical instability is not fully damped.

The dashed line shows the inverted rotation curve with the regularization parameter increased to 10^{-2}; the oscillations are considerably damped. The dotted line shows the results of the inversion with a regularization parameter of 1; here the result matches nearly precisely to the input rotation curve. In this figure, the departures of the inverted rotation rate from the input rate are small; all 21 modes indicated in Figure 3 were used in the inversion. Similar departures between the input and inverted rotation profiles were found for the rotation curves that increase and decrease linearly with radius.

The flat and linear rotation curves share the property that derivatives of $\boldsymbol{\Omega}$ higher than the second are zero; this matches the constraints that the regularization matrix places on the solution. Because of this it is no surprise that the inversion with regularization (and suitable regularization parameter) matches the input rotation curve. We examined splittings cause by the rotation curve shown in Figure 5, which is a power law in r/R with a power of -10. Computation of the inversion of the splittings for this rotation rate results in a very precise match with the input rotation curve, again using the PG 1159 model. On a linear scale in radius, the match is very good. Near the surface, the

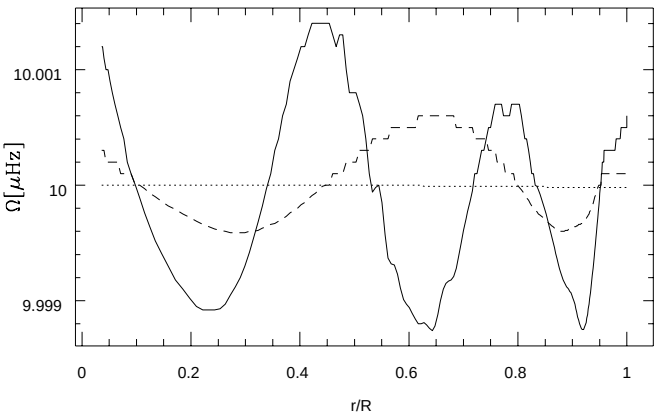

FIG. 8.—Results of regularized inversions of rotational splittings for the PG 1159 model with a flat rotation curve. The solid line is for a regularization parameter λ of 10^{-4}; the dashed line shows the inverted rotation profile for $\lambda = 10^{-2}$, and the dotted line is the inversion with $\lambda = 1$.

match is still very good, though the regularized solution is somewhat lower than the input rotation rate. This is because the inversion is enforcing a rotation curve that is flat and inflection free, while the true curve has nonzero derivatives at this point.

As a final example of the regularized inversion technique for the PG 1159 model, we attempted to invert the splittings in the case of a discontinuity in $\Omega(r)$. The results of this inversion are shown in Figure 9 for several different regularization parameters with the input rotation rate shown as a heavy line. In this situation, the inversion shows interesting behavior at the position of the discontinuity, but only at small values of λ. Increasing λ smooths the inverted rotation curve, resulting in better agreement with the input curve at the center and surface, but washing out the signal of the discontinuity at $r/R = 0.5$. In principle, the inversion could be better if we adapted the regularization matrix to allow for discontinuities.

Inversions for the GD 358 model with linear (or flat) rotation curves showed the same general features as for the PG 1159 model. However for rotation curves that do not share the properties of the regularization matrices, the difference between the input and inverted rotation rates was much greater than for the PG 1159 model. This is understandable, given that the rotation kernels for the GD 358 model are much larger near the surface; the inversions therefore are strongly constrained near the surface and much less at the center. Therefore, for rotation curves such as the power-law rotation curve, the inversions will try to fit the surface behavior at the expense of the interior. The response of the inversions to the splittings in the case of a discontinuity in $\Omega(r)$ show a similar pattern to that illustrated for PG 1159 modes when the discontinuity lies where the rotation kernels themselves are large (i.e., near the surface). When the discontinuity is below this region, the inversion procedure matches the flat rotation near the surface but becomes meaningless further in.

4.2. *Inversion of Splittings with Errors*

The experiments recounted above have used synthetic splittings with no errors. Of course, observed rotational splittings will contain errors because of the limited length of observing runs, pattern noise from imperfect sampling and multiple periods, and noise from photon statistics, seeing, and other effects. To examine the effects of observational errors on the inversions, we have added noise to the computed splittings and calculated regularized inversions for the PG 1159 model with a flat rotation curve. Results of this exercise are illustrated in Figure 10. The noise introduced was normally distributed (in frequency) with a standard deviation of 0.04 μHz, which is comparable with the best data available for pulsating white dwarfs as observed with the Whole Earth Telescope. Of course, the actual observed noise is not normally distributed (Costa & Kepler 1998), but we choose a normal distribution for illustrative purposes. The lower panel of Figure 10 shows a sample set of splittings with errors along with the noise-free splittings. The upper panel shows how the regularized inversion procedure reacts. Increasing the value of the regularization parameter λ smooths out the solution, as expected. With increasing λ the inversion approximates the noise-free value of a flat rotation rate of 10 μHz. However, it is clear that noise introduces false structure in the inverted rotation curve at the 10% level, even when the regularization parameter used is relatively large (0.1).

In the case of a nonflat rotation curve, the situation is more complicated. The top panel of Figure 11 shows the results for the rotation rate decreasing as the 10th power of

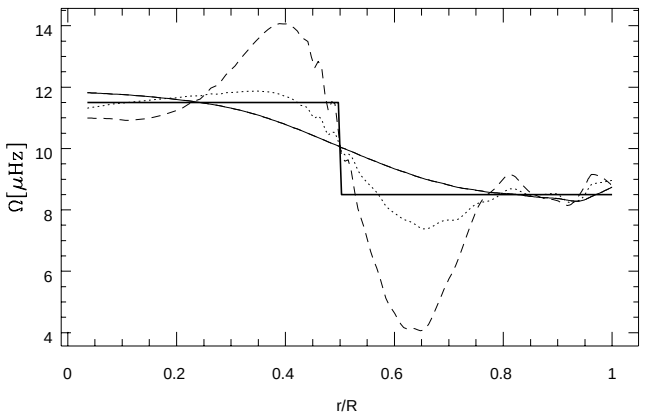

FIG. 9.—Regularized inversion for PG 1159 model with a rotation curve with a discontinuity at the half-radius point (*heavy line*). The inversions are with $\lambda = 10^{-4}$ (*dashed line*), $\lambda = 10^{-3}$ (*solid line*), and $\lambda = 10^{-2}$ (*dotted line*).

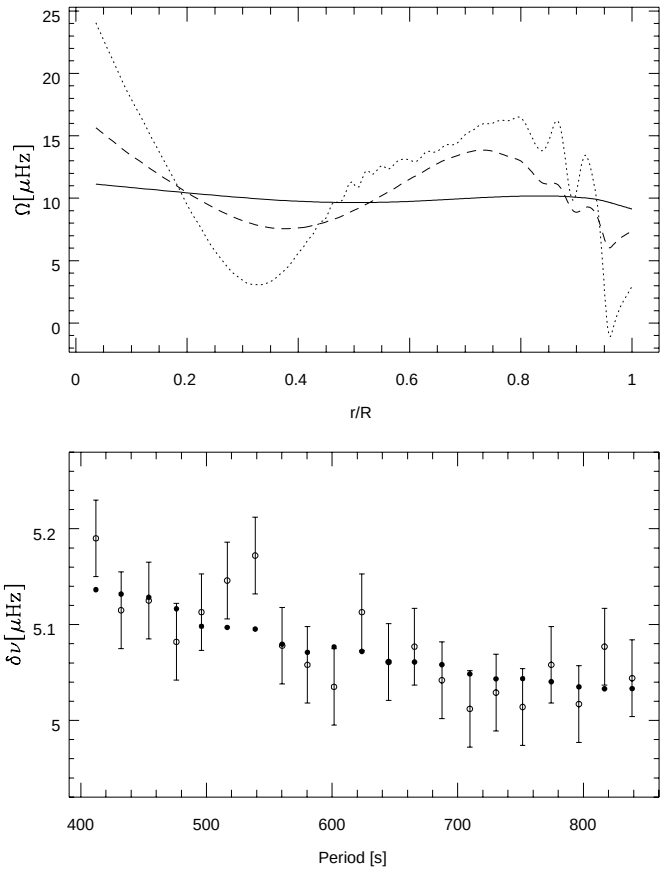

FIG. 10.—*Upper panel*: Inverted rotation curves for splittings computed with a flat rotation rate, but with noise added to the splittings. In this figure, the solid line signals the inversion with a regularization parameter of 0.1, the dashed line has $\lambda = 0.01$, and the dotted line has $\lambda = 0.001$. *Lower panel*: Splittings for a flat rotation curve with no noise (*filled circles*) and the same splittings with a normally distributed error of 0.04 μHz.

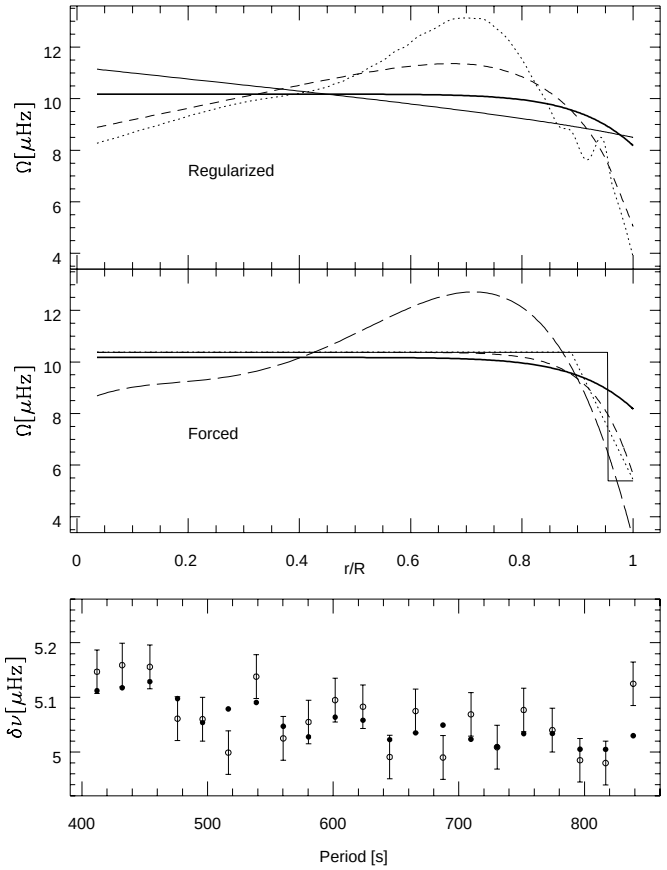

FIG. 11.—Inversions of splittings for the rotation curve from Fig. 5, but including synthetic errors for the splittings with a normally distributed error of 0.04 μHz. The input rotation curve is shown as a dark solid line in the top two panels. *Top panel*: Results of regularized inversions of the simulated splittings for $\lambda = 1$ (*thin solid line*), $\lambda = 0.1$ (*dashed line*), and $\lambda = 0.01$ (*dotted line*). *Middle panel*: Function fittings using the same splittings: polynomial rotation curve, degree 5 (*long-dashed line*), power-law rotation curve (*short-dashed line*), flat + linear (*dotted line*), and discontinuous rotation curve (*thin solid line*). *Bottom panel*: Error-free splittings (*filled circles*) and the splittings with simulated errors (*open circles with error bars*). The inversions shown in the top two panels all used splittings given by the open circles.

r/R; the input rotation curve is shown as a dark solid line in this figure. In this case, the regularized inversions do detect that the rotation rate decreases outward but do not converge to the proper form. Increasing the regularization parameter smooths the rotation curve further; it approaches to the input rotation curve, but with exaggerated structure. With a regularization parameter of 1, the departure from the true rotation curve is smallest, but strong regularization results in a rotation curve that drops nearly linearly with radius. This behavior was anticipated given the similarities of the splittings shown in Figure 5.

We next show how the function fittings behave with noisy splittings. The middle panel of Figure 11 illustrates function fittings of the same splittings. Because of the much smaller number of parameters being fit, this procedure should be a better choice in this case. Since the input rotation curve was one of the four forms used in the function fitting, this test may not be fully fair. However, inspection of the figure shows that all forms follow the general trend of the input rotation curve, but with exaggerated features. In this sense, the results are similar to the regularized inversion results. All show decreasing rotation rates in the outer layers, as was input, but all also decrease more than was input. However, the value of the rotation rate near the center is, for all but the polynomial case, much closer to the input value. Of the four forms, the form that gives a minimum value for χ^2 was the discontinuous case (*thin solid line* in Fig. 11).

In other cases, the function fitting gives more accurate results. Figure 12 show the results of inversions of the splittings (with errors) computed using the discontinuous rotation curve in the PG 1159 model. The regularized inversions (Fig. 12, *top panel*) show oscillatory behavior for small values of the regularization parameter. However, as λ is increased, the inverted rotation curve shows a proper decrease with increasing radius, though of course the smoothing results in a lack of resolution of the discontinuity. With function fittings, the smallest values of χ^2 are obtained for solutions using a discontinuous rotation curve; the best curve in the middle panel of Figure 12 is such an inversion and, despite the errors in the splittings, is a reasonably accurate representation of the input rotation curve.

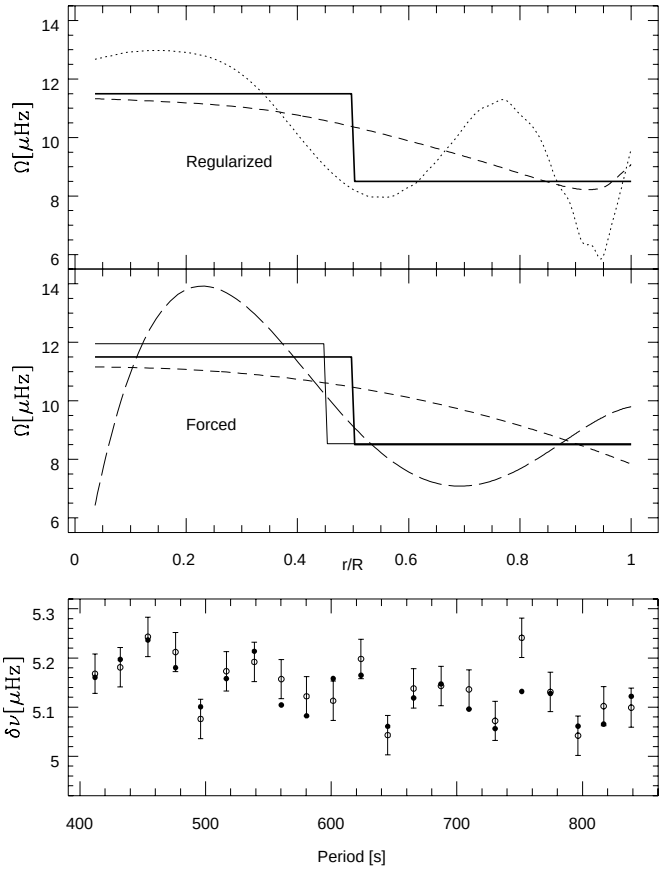

FIG. 12.—Inversion of splittings for a discontinuous rotation curve in a PG 1159 model. The input rotation curve is shown as a dark solid line in the top two panels. *Top panel*: Regularized inversion results with $\lambda = 0.01$ (*dotted line*) and $\lambda = 0.1$ (*dashed line*). *Middle panel*: Function fittings with the same splittings: 5th order polynomial (*long-dashed line*); power-law rotation curve (*short-dashed line*); the best value for the power in this case is 2.5; and best-fit rotation curve with a discontinuity (*thin solid line*). Of the three inversions shown, the discontinuous rotation curve had a minimum value of χ^2. *Bottom panel*: Forward-calculation splittings (*filled circles*) and splittings with synthetic errors (normally distributed over 0.04 μHz). Inversions shown in the top two panels all used splittings given by the open circles.

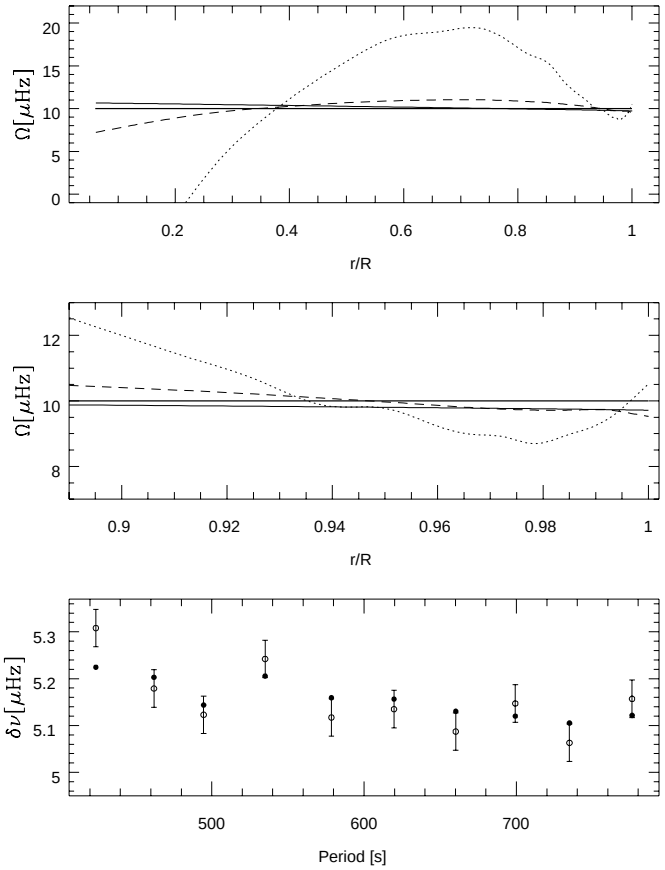

FIG. 13.—Inversions for rotational splittings from a flat rotation curve in the GD 358 model (*heavy solid line*), but with errors in the splittings derived from a normal distribution. *Top panel*: Inversions for $\lambda = 0.01$ (*dotted line*), 0.1 (*dashed line*), and 1.0 (*solid line*) through the entire model. *Middle panel*: Expansion of the radial scale for the outer layers. *Bottom panel*: Splittings used in the inversion.

In the GD 358 model, the presence of noise also degrades the inversion accuracy, as could be expected from examination of Figures 6 and 7. Figure 13 illustrates the magnitude of the problem for regularized inversions of the flat rotation curve splittings (with noise at the same level as in previous figures). The inverted rotation curves diverge quickly in the inner parts for small values of λ, but even near the surface (where the kernel values are largest) the inverted rotation curves are markedly different from flat. Only for λ near 1 is the inverted rotation curve similar to the input value. For the function fittings, the results also are sensitive to the errors; for this inversion technique, the best-fit rotation curve is flat through 98% of the interior at a rotation rate of 10.1 μHz and then decreases to about 8.7 μHz at the surface.

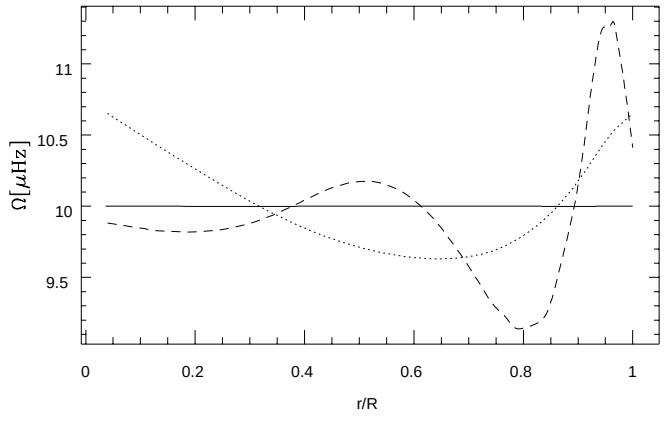

FIG. 14.—Regularized inversions of noise-free splittings of the PG 1159 model using "incorrect" kernels taken from a later model in the evolutionary sequence. The solid line shows the regularized inversion of the correct model with $\lambda = 0.01$; the dashed line is the inversion with the incorrect model with the same value of λ. The dotted line shows the inversion with $\lambda = 0.1$; there is no significant improvement in increasing λ.

4.3. *Errors in the Equilibrium Model*

Another possible source of error is in the background equilibrium model used for the inversion: if it is not an accurate representation of the star, then the inverted rotation curve will be in error. To illustrate the uncertainties that can arise in the inversion procedures from this effect, we recomputed regularized and function fittings for the flat rotation curve in the PG 1159 model, but using a different model for the inversions. In this test, we used a more evolved model (with $T_{\rm eff} = 117{,}100$ K, compared to 134,400 K for the basic model). This cooler model shows rotation kernels that are more concentrated in the outer layers than the original model; the periods and trappings are sufficiently different from the first model that it would not necessarily be considered an equivalent fit. This model represents a "poor fit" to the periods of the main model but allows us to judge the effects of the assumed model on the reliability of the results. Figure 14 shows the results of regularized inversions given the error-free splittings from a flat rotation curve. The splittings are from the original model. Clearly, even with a relatively large regularization parameter, the poor model shows significant structure in the inverted rotation curve that is entirely caused by its improper kernels.

Given the results for these tests, it appears that the function fitting technique gives reasonably accurate results for the PG 1159 model in the presence of noise. However, it is essential to have a very good initial equilibrium model that reproduces the observed periods and period spacings as precisely as possible.

5. APPLICATION TO OBSERVED SPLITTINGS IN WHITE DWARFS

The techniques we have explored show that reliable inversions require a number of accurately measured frequency splittings. The larger the number of splittings, and the larger the range of n, the better. To date, only three white dwarf stars have had multiple rotational splittings measured. These are the GW Vir stars PG 1159 and PG 2131, and the DB white dwarf GD 358. Figure 15 shows the splittings for PG 1159 and GD 358.

PG 1159 is the reigning champion, with rotational splittings of 20 $l = 1$ modes tabulated by WWETPG. Of those 20, nine multiplets have some uncertainties associated with them, either because the multiplets are identified within the noise using the spacing constraints or because other mode identifications are possible. The measured splittings are the same to within the measurement error. This suggests that PG 1159 does not have significant differential rotation. Kawaler et al. (1995) report that PG 2131 shows six triplet modes, with some uncertainties in splittings because of fine structure in the high-frequency component of the triplets.

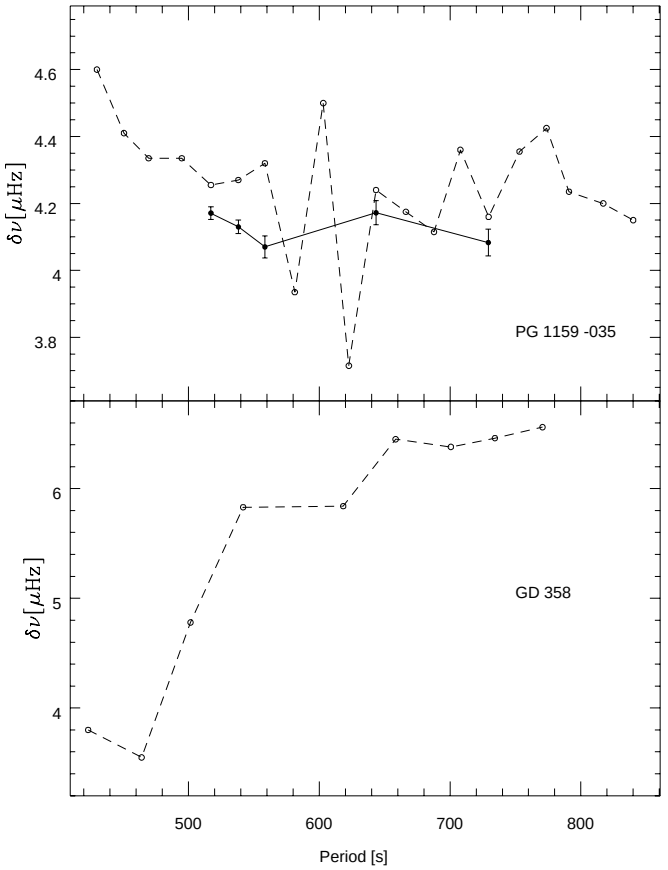

FIG. 15.—Observed frequency splittings for (*upper panel*) PG 1159 and (*lower panel*) GD 358. The two sets for PG 1159 represent the splittings derived in WWETPG from the power spectrum directly (*open circles*) and by the least-squares fitting procedure described in the text (*filled circles*). The splittings for GD 358 are from the power spectrum analysis of WWETDB.

The DB white dwarf GD 358 shows nine triplet modes in the analysis by WWETDB. These show a wide range of splittings, with the splittings of low-n modes being a factor of 1.6 times smaller than for higher n modes. The simple interpretation, described by WWETDB, is that GD 358 has a slowly rotating core.

In this section, we apply the tools derived above to the observed spacings in PG 1159 and GD 358. As we show, the published splittings in these cases contain small frequency errors that are fatal to the inversion procedure. By reanalysis of the original data for PG 1159, however, we use what we have learned through the forward problem to show that this star shows a rotation rate that declines with radius. We also show that the published splittings for GD 358 are suggestive of differential rotation but that the situation is more complex than suggested by WWETDB.

5.1. *PG 1159*

For PG 1159, our starting point is the table of frequencies for PG 1159 published in WWETPG. They used the strongest triplets in the power spectrum to determine an initial estimate of the period spacing and mean rotational splitting. Armed with these, they then dug deeply into the power spectrum to identify low-amplitude modes. As a consequence of this analysis, they were able to identify probable members of the $l = 1$ spectrum; however, these low-amplitude modes had comparable amplitudes to that of the noise in the spectrum. Since frequency errors in the splittings can cause large errors in the inversions, we cannot include these low-amplitude modes in the inversion procedures. Furthermore, WWETPG point out that some of the $l = 1$ components may be identified incorrectly.

Another problem with the published frequencies is that they were determined directly from the computed power spectrum. Therefore, neighboring peaks (whether from noise or from the star) can "pollute" one another and cause small errors in the frequency determinations for nearby peaks. Though the spectral window was extremely good for this Whole Earth Telescope run, residual aliases can also affect the accuracy of frequency determinations when made directly from the power spectrum. One way to solve this problem is to do a nonlinear least-squares solution for the amplitude, frequency, and phase for all peaks in the spectrum simultaneously. This procedure was used by Kawaler et al. (1995) for PG 2131 and is described in more detail in O'Brien et al. (1996). As long as one is careful not to allow the nonlinear least-squares procedure to converge on a local minimum in χ^2, then this procedure allows one to find the frequencies of each peak as if it were isolated; that is, the effects of sampling and pollution by other peaks are removed.

To illustrate this influence, we show in Table 1 the frequencies for several modes in PG 1159 obtained from WWETPG and from a simultaneous nonlinear least-squares fit to their data. In the least-squares solution, only the modes near clearly identified triplets were included; without modes present that are clearly above the surrounding noise level, least-squares solutions suffer from the same problem of noise pollution. The amplitudes in this table are in milli–modulation amplitudes; one mma is $\delta I/I$ of 10^{-3}. Even though the differences in frequency are small (from a model-fitting perspective), the splittings are significantly different. Other interesting features of this comparison are the amplitudes are significantly reduced in the largest peaks and that the relative amplitudes are different. This is caused by overlapping of the windows of these strong peaks. The fact that the amplitude ratios change in the least-squares analysis is important for interpretation of the amplitudes of the separate m components in terms of inclination of the rotation/pulsation axis. Figure 15 shows the splittings computed via least squares as solid dots connected by a solid line.

Using the frequencies in Table 1, we computed the regularized inversions for PG 1159 using a best-fit model that was very similar to the model of Kawaler & Bradley (1994). This is not the model that was used for the tests in previous sections but is optimized to fit the periods and period spacings of PG 1159 itself. Figure 16 shows the regularized inversions of the splittings with λ of 0.01, 0.1, and 1.0. The inversion with the smallest λ shows what looks like spurious structure, based on tests with sample data. With a larger λ, the rotation curve appears to decrease with increasing radius, with some small contrast. Is this real?

If so, it should also manifest itself in the function fittings. All of the forms for the rotation law minimize χ^2 when the surface rotation rate is smaller than the central value; the best fit of the three forms is the discontinuous rotation curve, with a surface rotation rate of about 7 μHz and a central (within the inner 20% of the radius) rate of about 12

TABLE 1

FREQUENCIES AND SPLITTINGS IN PG 1159

	WWETPG			LEAST SQUARES		
n	Frequency (μHz)	Amplitude (mma)	$2\langle\delta\nu\rangle$ (μHz)	Frequency (μHz)	Amplitude (mma)	$2\langle\delta\nu\rangle$ (μHz)
32.....	1367.11	1.00		1367.15 ± 0.05	0.94 ± 0.07	
	1370.80	0.56	8.32			8.17 ± 0.08
	1375.43	0.81		1375.32 ± 0.06	0.74 ± 0.07	
28.....	1550.39	1.07		1550.43 ± 0.05	0.87 ± 0.07	
	1554.23	0.55	8.49			8.34 ± 0.07
	1558.88	1.18		1558.77 ± 0.05	1.00 ± 0.07	
24.....	1786.24	1.29		1786.70 ± 0.06	0.85 ± 0.09	
	1790.70	2.46	8.64	1790.67 ± 0.02	2.53 ± 0.08	8.14 ± 0.07
	1794.88	3.30		1794.84 ± 0.02	3.01 ± 0.09	
23.....	1854.04	6.10		1854.06 ± 0.01	5.43 ± 0.09	
	1858.20	4.16	8.54	1858.20 ± 0.01	3.82 ± 0.08	8.26 ± 0.04
	1862.58	2.73		1862.32 ± 0.04	1.45 ± 0.09	
22.....	1929.32	5.09		1929.44 ± 0.02	3.57 ± 0.09	
	1933.55	4.25	8.51	1933.61 ± 0.01	3.87 ± 0.08	8.34 ± 0.02
	1937.83	6.87		1937.78 ± 0.01	6.27 ± 0.09	

μHz. These numbers are inherently uncertain; such a rotation law is simply consistent with the small number of splittings within the errors of the splittings.

These indications of a decreasing rotation rate from the center to the surface are model dependent; a slightly different model for PG 1159 that matches the periods nearly as well could indeed produce a quantitatively different rotation curve. However, Figure 3 shows a way in which we can estimate the sign of the slope of the rotation curve without recourse to detailed models. The general features of that figure was that a rotation curve that decreases with radius shows variations in $\delta\nu$ that are out of phase with the variations for a rotation curve that increases with radius. Mode trapping, as is manifest in departures from uniform period spacings, provides the key. Figure 4 shows the variations of $\delta\nu$ for a rotation rate that decreases with increasing radius compared with departures from uniform period spacing (backward differenced). When the rotation rate decreases with radius, the variations in $\delta\nu$ are largely in phase with the variations in ΔP. For an increasing rotation curve, then, the variations in $\delta\nu$ will be out of phase with variations in ΔP.

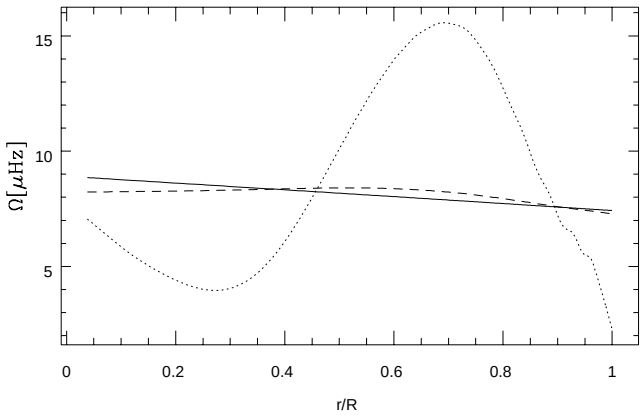

FIG. 16.—Regularized inversions of the actual splittings from PG 1159 for $\lambda = 0.01$ (*dotted line*), 0.1 (*dashed line*), and 1.0 (*solid line*).

Therefore, for PG 1159 and any other star that shows a sufficient number of consecutive overtones, plotting the frequency spacing and period spacings together allows determination of whether the rotation rate increases or decreases with depth, without recourse to detailed models. Such a plot is shown in Figure 17; the decreasing splittings between 500 and 580 s fall in parallel with the decreasing period spacings.

5.2. *GD 358*

GD 358, the prototype of the pulsating DB (helium-atmosphere) white dwarfs, has been observed by the Whole Earth Telescope twice. The first WET campaign, of 1990 May, was described in detail by Winget et al. (1994). We did not perform a complete least-squares analysis of the data from this campaign. As a result, we will not attempt to determine if the splittings are in phase with the period spac-

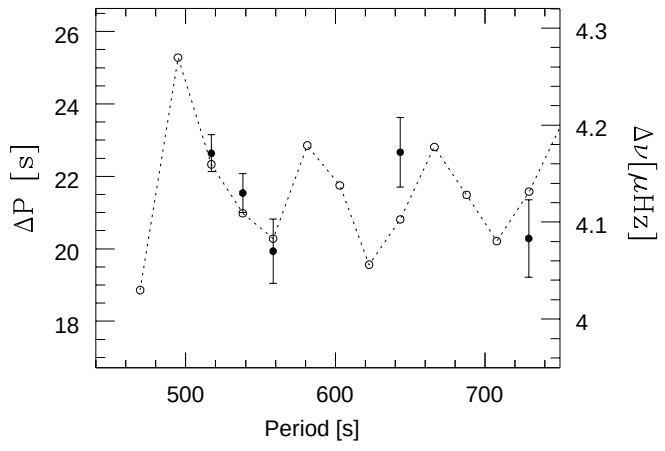

FIG. 17.—Period spacing as a function of period for the $l = 1$ modes identified by WWETPG (*dotted line*, l*eft-hand scale*); data points show the observed rotational splittings (*right-hand scale*). Note that the rotational splittings and period spacings change in phase. This suggests that the rotation rate decreases with radius in PG 1159.

ings, as was possible with the PG 1159 data. The increase in rotational splitting on pulsation period that WWETDB deduced from the power-spectrum analysis (see Fig. 15) will probably not change dramatically with a reanalysis. The two shortest period modes show splittings between 3 and 4 μHz, while the longer period modes have splittings of about 6.4 μHz. The results of our experiments with the forward analysis (see Fig. 7, for example) suggest that producing such a large contrast in splittings requires a very steep change in the rotation rate in the stellar interior. The model of GD 358 that we use to obtain kernels and attempt inversions is described in Dehner & Kawaler (1995); it represents a good match to the observed periods, effective temperature, and luminosity of GD 358.

As a first approximation, we try to invert the observed splittings using function fitting. Contrary to expectation, the best-fit rotation curves show a rapidly rotating inner core, with the discontinuity at a fractional radius near 0.2. For a discontinuous rotation curve, the best fit is for an inner rotation frequency of 140 μHz (out to $r/R = 0.20$) with the rotation rate in the remainder of the model of 0.6 μHz. A similar quality fit was found for a rotation rate of 280 μHz at the center, decreasing linearly to 0.25 μHz at a fractional radius of 0.22 and remaining constant out to the surface. A somewhat similar rotation curve is found through a regularized inversion [with constraints on the first and second derivatives of $\Omega(r)$].

Figure 18 shows the results of a representative solution; the upper panel shows the rotation curves resulting from a function fitting and from the regularized inversion (with $\lambda = 10^{-2}$). The lower panel shows a comparison of the observed splittings with the model splittings, computed with a forward calculation, for the rotation curves in the upper panel. Clearly, the regularized inversion provides an unphysical rotation curve—a negative rotation velocity through much of the interior—despite producing splittings that match the observed splittings quite well. The feature of the rotation curve that causes the low-n modes to have smaller frequency splittings is the steep decrease in Ω in the inner regions.

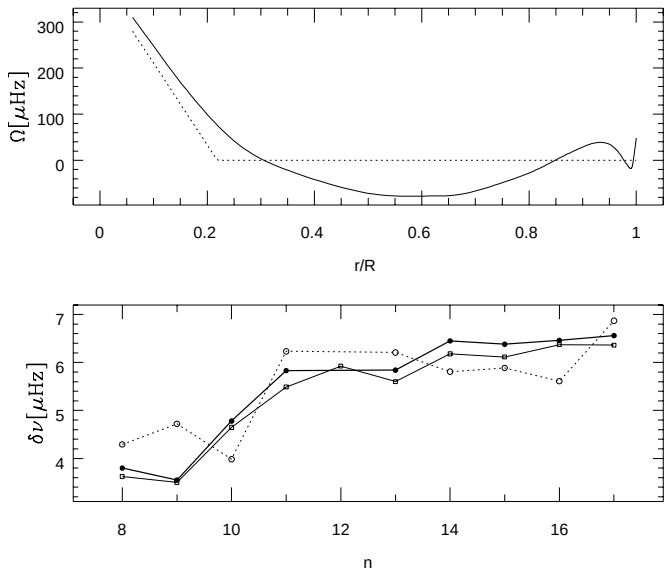

FIG. 18.—Results of inversions of the observed frequency splittings of GD 358. *Upper panel*: Results of a regularized inversion ($\lambda = 10^{-2}$; *solid line*) and the results of a function fitting (linear inside, flat outside; *dotted line*). *Lower panel*: Splittings computed for the given rotation curves. The dark solid line shows the observed splittings.

The reason why the inversions result in a rapidly rotating inner region result from the combined effects of the behavior of K near the center and the effects of mode trapping. We illustrate these effects in Figure 19. Figure 19*a* shows the running integral $\int_0^r K_i(r')\,dr'$ as a function of r for selected $l = 1$ modes in our model of GD 358. Figure 19*a* shows the integral over the entire model for the trapped mode $n = 9$, the untrapped mode $n = 13$, and the trapped mode $n = 15$. The splitting of the $n = 9$ mode in GD 358 is 3.6 μHz, while the splitting of the other two modes are 6.4 μHz. Figures 19*b* and 19*c* show the integrated kernels near the center and surface.

Figure 19*b* shows that the higher n modes have larger integrated kernels than the $n = 9$ mode. Within $r/R = 0.2$, the $n = 13$ and $n = 15$ modes have nearly identical values, which are about 40% larger than the value for the $n = 9$ mode. This turns out to be the dominant factor that causes the inversion procedures to demand a rapidly rotating core. By isolating fast rotation in these inner regions, the inverted rotation curve can produce large splittings for the higher n modes. However, because these inner regions contribute only 5% of the total splitting, the inner rotation rates required are quite fast (see Fig. 18).

The secondary effects of mode trapping are illustrated in Figure 19*c*. The three low-n modes ($n = 8$, 9, and 10, with $n = 9$ shown in the figure) are trapped modes that show a large maximum in the rotation kernels near the surface. Therefore, these modes sense the outer regions more than the untrapped modes ($n = 11$–13, with $n = 13$ shown in Fig. 19*c*). If the outer region is rotating much more slowly than the inner region, then the trapped modes will show smaller splittings than untrapped modes. For the next set of trapped modes ($n = 14$–16, $n = 15$ shown in Fig. 19*c*), the maximum value of the rotation kernel is concentrated farther out than the lower n trapped modes. Therefore, integrating these kernels over the narrower region has a smaller impact on the splittings, and the higher n trapped modes show larger splittings than the lower n trapped modes (beyond the effects of the central regions described above.

It is not at all clear how realistic the results of these inversions are for GD 358; the numerical procedures attempt to utilize the small (in an absolute sense) differences in the kernels near the center to minimize χ^2 while most of the action in the pulsations is near the surface. If we confine our inversions to adjust Ω in the outer regions only, can the inversions do nearly as well? Using function fittings with discontinuous rotation curves, we show in Figure 20*a* the value of χ^2 as a function of the fractional radius of the discontinuity. The deepest minimum is at a fractional radius of 0.2 and corresponds to the discussion above. However, there is a deep local minimum in χ^2 in the outermost layers. The corresponding solution has a rotation frequency of 8.4 μHz from the center to a fractional radius of 0.9974; the rotation frequency increases discontinuously to a surface rate of 66 μHz.

Note that this outer solution suggests a quickly rotating surface, while the inner solution indicates a quickly rotating core! Figures 20*b* and 20*c* show the splittings that result from these solutions, along with the data from GD 358. The near-surface discontinuity does produce splittings that are as close to the observed splittings as those from the deep

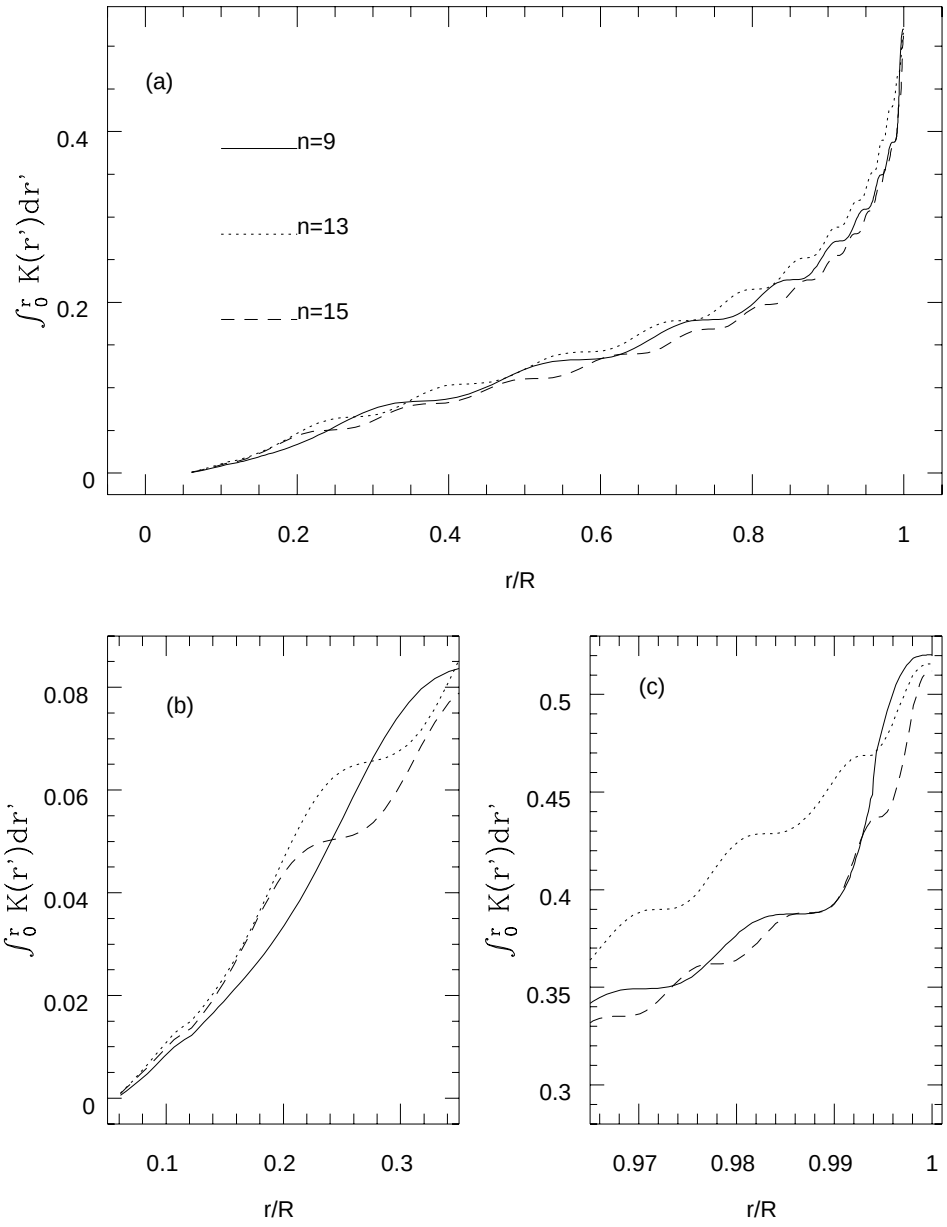

FIG. 19.—Running integral of the rotation kernel for selected modes in the GD 358 model. The ordinate shows the value of the integral up to the value at the abscissa; the value at $r/R = 1$ corresponds to $1 - C_{nl}$. Integral over (*a*) the entire interior, (*b*) the central regions, and (*c*) the outer layers.

discontinuity. Since the observed splittings that we used in this study are taken from the power-spectrum analysis of WWETDB, it is still to early to claim with any certainty that GD 358 has either a rapidly rotating core or a rapidly rotating outer envelope. Additional complications, including the possible effect of magnetic fields on the observed splittings in GD 358 (WWETDB; Jones et al. 1989) further complicate the picture.

6. CONCLUSIONS: PROSPECTS FOR FUTURE INVERSIONS

This investigation has shown that even though the information provided by the pulsations of white dwarf stars is much less extensive than that provided by solar oscillations, some pulsators are rich enough to constrain their internal rotation. The technique of regularized inversion is of limited use under even these circumstances but can provide insights into the oscillation properties of models of these stars. Function fitting, where the inverted rotation profile is constrained to fit simple functional forms, represents a useful alternative.

For the pulsating white dwarf stars, very accurate pulsation frequencies are needed to allow constraint of the rotation curve. We explored the data on PG 1159 and were able to demonstrate that the rotational splittings are sensitive to mode trapping. In fact, we show that the phase between the rotational splitting and period spacings (as functions of period) allows an observational determination of the sign of the slope in the rotation rate with depth. PG 1159 shows the signature of a rotation curve that is faster at the center than at the surface. Further observations of this star by the Whole Earth Telescope are now available (D. E. Winget 1998, private communication); least-squares analysis of these data, in combination with the first WET data on this star, should be able to test this result.

The case of the pulsating DB white dwarf GD 358 is interesting as well. The data available in the literature indi-

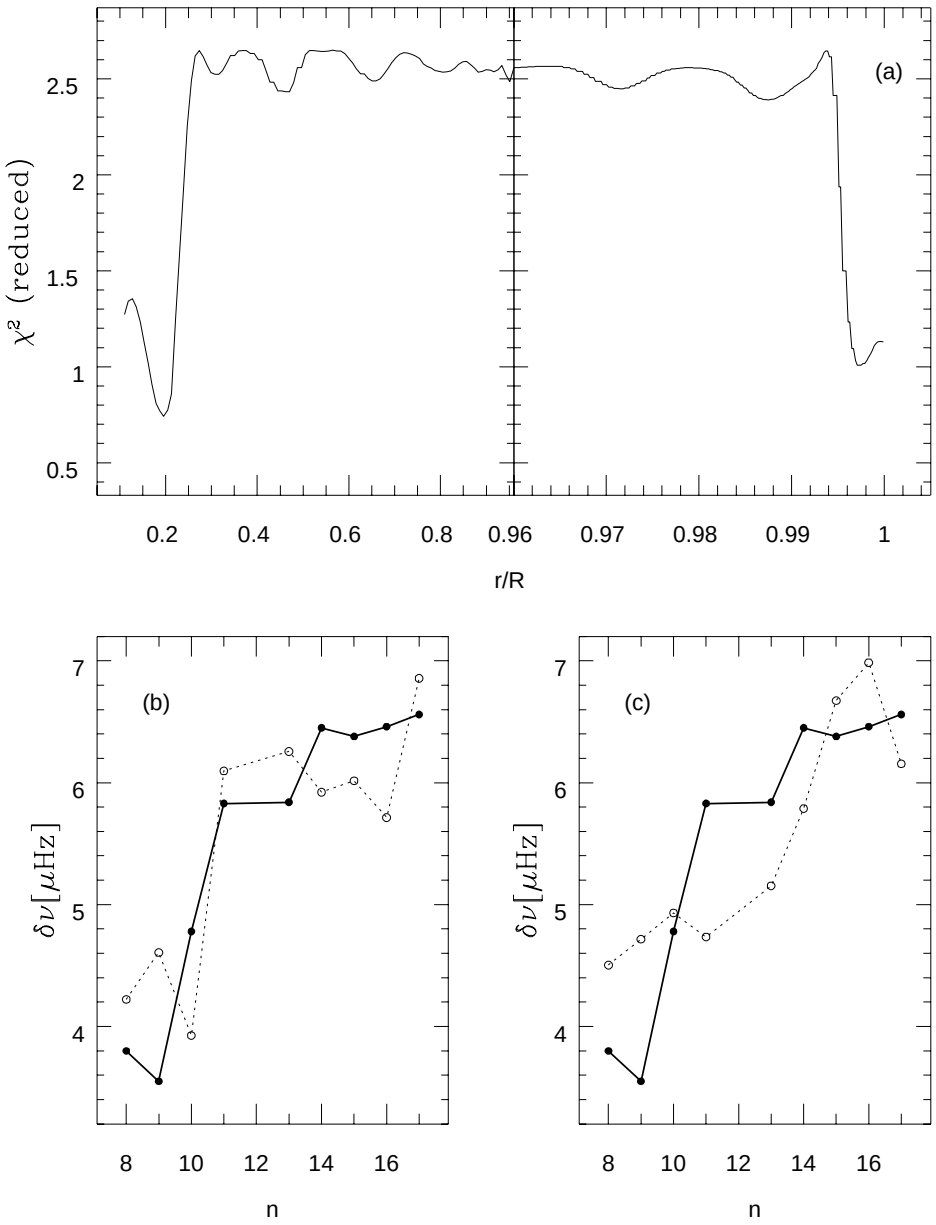

FIG. 20.—(*a*) Run of χ^2 for the function fitting of the GD 358 splittings with a discontinuous rotation curve. The *x*-axis shows the position of the discontinuity; the outer regions of the model are on an expanded horizontal scale. The computed splittings with the inverted rotation curve (*dotted line*) are compared with the observed splittings (*solid line*) for (*b*) the solution corresponding to the inner minimum of χ^2 and (*c*) the outer minimum.

cate that this star does not rotate as a solid body. The rotation kernels from Figure 2 and the experiments described in this paper illustrate that earlier interpretation that the lower n modes sense the interior more than the higher n modes (which is what led WWETDB to conclude that the outer layers of GD 358 rotate faster than the inner layers) is oversimplified. As we show, the observed spacings can be reproduced if the star has a rapidly rotating inner ($r/R < 0.2$) core or, with a bit less accuracy, if it has a rapidly rotating outer surface (the outer $0.003R_*$). Clearly, we need to reanalyze the data from the two WET campaigns on this star with the least-squares technique to obtain more accurate pulsation frequencies and splittings.

S. D. K. acknowledges the National Science Foundation for support under the NSF Young Investigator Program (Grant AST-9257049) to Iowa State University and the NASA Astrophysics Theory Program through award NAG5-4060. He is also very happy to thank the Institute of Astronomy and Churchill College, Cambridge University, for their hospitality and support during his visit. T. S. is grateful for the support by the Particle Physics and Astronomy Research Council. Mike Montgomery of the University of Texas provided several helpful comments on this paper, and we also benefited from helpful discussions with Wojtek Dziembowski.

REFERENCES

Bradley, P., & Winget, D. 1994, ApJ, 430, 850
Brickhill, A. J. 1975, MNRAS, 170, 404
Christensen-Dalsgaard, J., Schou, J., & Thompson, M. 1990, MNRAS, 242, 353
Costa, J. E. S., & Kepler, S. O. 1998, in Fourth Whole Earth Telescope Workshop Proc., Baltic Astron. ser. 7, ed. E. G. Meistas & P. Moskalik (Vilnius: Institut. Theor. Phys. Astron.), 83
Dehner, B. T., & Kawaler, S. D. 1995, ApJ, 445, L141
Gough, D. O. 1985, Sol. Phys., 100, 65
Gough, D. O., & Thompson, M. J. 1991, in The Solar Interior and Atmosphere, ed. A. N. Cox et al. (Tucson: Univ. Arizona Press), 519
Goupil, M.-J., Dziembowski, W. A., Goode, P. R., & Michel, E. 1996, A&A, 305, 487
Hansen, P. C., Sekii, T., & Shibahashi, H. 1992, SIAM J. Sci. Stat. Comput., 13, 1142
Jones, P. W., Pesnell, W. D., Hansen, C. J., & Kawaler, S. D. 1989, ApJ, 336, 403
Kawaler, S. D., & Bradley, P. A. 1994, ApJ, 427, 415
Kawaler, S. D., et al. 1995, ApJ, 450, 350
Kleinman, S. J., et al. 1998, ApJ, 495, 424
Koester, D., Dreizler, S., Weidemann, V., & Allard, N. 1998, A&A, 338, 612
Meistas, E., & Moskalik, P. 1998, Fourth Whole Earth Telescope Workshop Proc., Baltic Astron. Ser. 7 (Vilnius: Institut. Theor. Phys. Astron.)
Meistas, E., & Solheim, J.-E. 1996, in Third Whole Earth Telescope Workshop Proc., Baltic Astron. ser. 4 (Vilnius: Institut. Theor. Phys. Astron.), 105
Nather, R. E., Winget, D. E., Clemens, J. C., Hansen, C. J., & Hine, B. P. 1990, ApJ, 361, 309
O'Brien, M. S., Clemens, J. C., Kawaler, S. D., & Dehner, B. T. 1996, ApJ, 467, 397
Pilachowski, C., & Milkey, R. W. 1984, PASP, 96, 821
Schmidt, G. 1995, Rev. Mexicana Astron. Astrofis., 8, 147
Winget, D. E., et al. 1991, ApJ, 378, 326 (WWETPG)
———. 1994, ApJ, 430, 839 (WWETDB)